

Extracting Band-tail Interface State Densities from Measurements and Modelling of Space Charge Layer Resistance

Mingzhe Yu¹, Shona McNab¹, Isabel Al-Dhahir¹, Christopher E. Patrick¹, Pietro P. Altermatt², and Ruy S. Bonilla^{1*}

¹Department of Materials, University of Oxford, Oxford, OX1 3PH, United Kingdom

²Trina Solar, State Key Laboratory for Photovoltaic Science and Technology (SKL PVST), Xinbei District, Changzhou, Jiangsu Province 213031, China

Abstract- Dielectric-silicon interfaces are becoming ever more important to device performance. Charge inside a surface dielectric layer is neutralized in Si leading to an accumulation or inversion layer of free carriers. Additionally, states at the interface are occupied by charges via Shockley-Read-Hall carrier statistics. It is accepted that the density of interface charge near midgap, which can only reach a concentration as high as the density of states, D_{it} , has a minor effect on band bending compared to the charges in the dielectric for a well passivated interface. Here, we show that it is the state density near the band edge what plays the major role. We conclude this by comparing our measurements with device modelling of a Si/SiO₂ interface. We measure the wafer sheet resistance while applying various amounts of positive charge to the passivating dielectric on an n-type Si wafer, and then reproduce the measured resistance values using simulations. This modelling indicates that D_{it} at midgap has indeed a minor effect on the changes of the resistance, while tail states have a significant impact on the distribution of induced carriers. We test this model on five groups of differently passivated specimens. This method allows a sensitive detection of the concentration of donor- and acceptor-like states in the unavoidable band-tails. While we report on the Si/SiO₂ interface due to its relevance in photovoltaics, our method can be generally used to study the properties of other semiconductor-dielectric interfaces. As such this work is of importance across various interfaces in optoelectronic devices.

Keywords: interface state density, dielectric surface passivation, field-effect, silicon-silicon dioxide interfaces

* Corresponding author: sebastian.bonilla@materials.ox.ac.uk

1 Introduction

The interface defect state density is a critical property of semiconductor-dielectric interfaces. Since these states have their energy levels in the bandgap, they can therefore act as strong recombination centres or store large concentrations of charge, both of which may be detrimental to photovoltaics devices [1]. Fundamentally, these states are formed as a result of the breaking of translational symmetry when the two bulk materials are brought together to form an interface. However, the precise origin of these states and their role in device physics has been the subject of study for many decades (see Ref. [2] for a review). The states can be classified broadly as either intrinsic or extrinsic [3]. The extrinsic states require the formation of defects such as vacancies, interstitials, or impurities. These defects can create bound states whose energies depend precisely on the perturbation to the potential due to the structural and/or electronic properties of the defect [4]. In terms of device performance, extrinsic defects can give rise to localized states with energies lying towards the middle of the gap and are hence problematic [5]. These deep levels act as traps for electrons, greatly increasing the probability of recombination and decreasing the carrier density.

In the intrinsic case, terminating the periodicity of the bulk material leads to a continuum of exponentially decaying (evanescent) states whose energies lie in forbidden band gap of the bulk material. These states were first introduced in the context of metal-semiconductor junctions [6]. As indicated by the name, they are an intrinsic and fundamental property of the material. They can be understood as Bloch states of the bulk semiconductor with complex wave vector [7], and can be viewed as having valence or conduction band character depending on their energies. Often the large density of these states at the interface provides an effective mechanism to pin the Fermi level and explain the energy-level alignment at semiconductor interfaces [7]. The effect of intrinsic states on the energy levels at the interface, conveniently characterised through the density of states D_{it} , is more continuous in nature. As an illustration, consider the first-principles density-functional theory calculations of layer-resolved density-of-states for a defect-free Fe/GaAs interface as reported in [8]. They show how the interface broadens the GaAs band edges such that they form tails which decay exponentially with energy towards the middle of the gap. A more pertinent example are calculations on model Si/SiO₂ interfaces which demonstrate the evolution of the band structure as one moves between the Si and SiO₂ regions [9,10].

Altogether, the interface states have a distribution of energy at different sections of the bandgap [11], which affect interface properties in different manners. For example, there is an asymmetry in probability for capturing an electron or hole, quantified as cross-section of electron or hole capture, σ_n and σ_p respectively, in units of cm². Near midgap, the Coulomb interaction of charged defect states usually dominates the recombination activity in covalently bond semiconductors like silicon. Near the band edges on the other hand, the shape of the atomic orbitals often plays a significant role. Whether a defect state acts as an effective recombination centre does not only depend on its σ_n and σ_p , but also on the Shockley-Read-Hall (SRH) statistics [12,13]. For example, both an electron and a hole must be captured for recombination to happen, and the less likely carrier limits the recombination rate. In the shallow defects at the band tails the re-emission probability of one carrier is large, deeming these states often inefficient for recombination except at very high dopant density, very high injection density, or substantial band bending [12,13]. Therefore, interface states at midgap are the primary concern for achieving high surface passivation. Such midgap D_{it} continues to be intensively studied and is nowadays widely used as a metric for surface passivation [14–16].

The fundamental properties of band-tail states, on the other hand, were only studied experimentally in the 1980s and 1990s [11,17–23]. An exponential increase in density towards conduction/valence band edge was observed in such works, in agreement with theoretical calculations. A consolidation of known Si/SiO₂ interface state densities in the literature, including band tails, is shown in Figure 1. It is clear that processing conditions can largely affect the interface properties, and that much fewer data exists for the true densities in the tails. Due to the relatively low recombination rate in such band-tail states, they have not been as prominently studied as the midgap strong recombination states. Despite this lack of attention, state density at band-tail can be several orders of magnitudes higher than that at midgap, and such band-tail states are able to store large concentrations of charge. These charges can alter the carrier distribution close to the interface via field-effect, and therefore influence surface passivation [24], and performance of devices involving a field-induced junction like inversion layer cells [25–27], metal-oxide-semiconductor field-effect transistors (MOSFETs) [28], and field-induced photodiodes [29]. The effect of band-tail state density on emitter conductivity of an inversion layer cell, and subsequently cell performance, has been evaluated and proved significant by simulations in our previous work [25]. The detection of the state density at band-tails is therefore necessary for understanding and manipulating

carrier distribution at the interface, and it can point new directions for improvement of devices involving field effect.

Capacitive techniques are reliable for detection of state density at midgap, while lacking sensitivity on the states at band-tail [18,30]. Surface photovoltage can be used to acquire state density across the whole bandgap, but with compromised accuracy at band-tails where the state density varies significantly in terms of energy [18]. Electron paramagnetic resonance spectroscopy is capable of detecting the states for such defects that are paramagnetic, for example, silicon dangling bonds at the Si/SiO₂ interface [31] and the Si/SiN_x interface [32], which correspond to the states at midgap rather than at band-tails [17]. No technique has yet been developed which can quantify the band-tail states with high sensitivity. In this study, we explore the effect that interface states both at midgap and in the band-tails have on the distribution of charge-induced electrons near a Si/SiO₂ interface. Such understanding allows us to propose a novel method of extracting the interface state density at band-tails from changes in the space charge layer, with the assistance of numerical simulations.

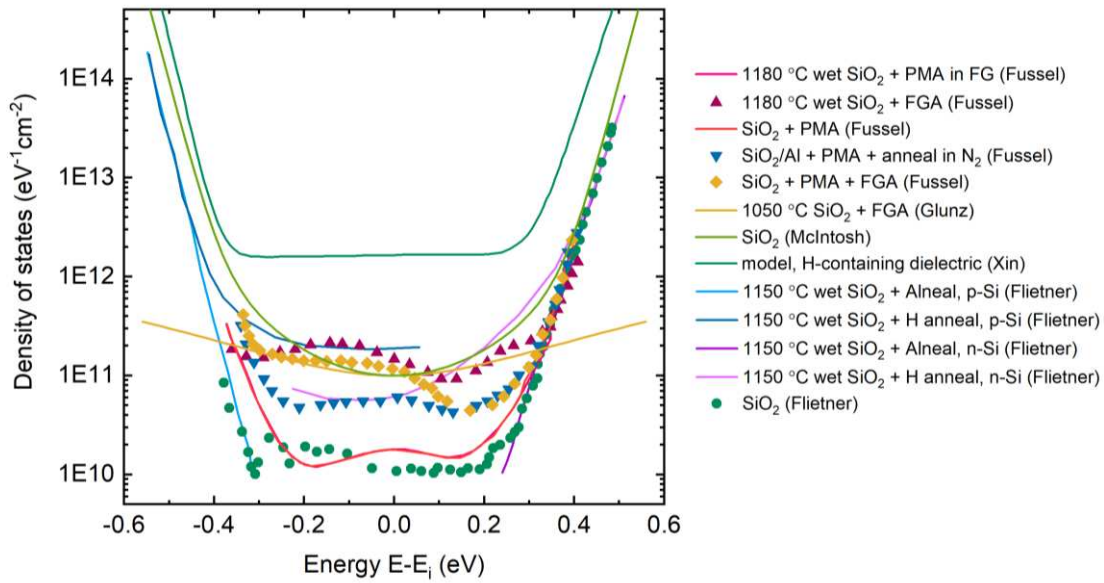


Figure 1. Density of states distribution of various Si/SiO₂ interfaces, redrawn from [11,17,20,22,23,33]. PMA: post metallization anneal; FGA: forming gas anneal; FG: forming gas.

2 Sample Preparation and Characterisation

Two sets of silicon wafers are used in this work with their band-tail state density characterised to demonstrate the potential of the interface characterisation method studied here. Set 1 starts with a 200 μ m thick, 1 Ω cm, phosphorus-doped n-type planar float zone, (100) silicon substrate. Three subset samples originate from Set 1 for a diversity of interfaces. Subset 1.1 has a 100 nm of thermal oxide grown on both sides at 1050 °C in a dry atmosphere. Some of Subset 1.1 wafers were subsequently forming gas annealed (FGA) in 5% hydrogen ambient at 425 °C for 30 min for enhanced chemical passivation, referred to as Subset 1.2. Subset 1.3 samples have a 10 nm of thermal oxide grown on both sides at 950 °C in a dry atmosphere and were annealed in 5% hydrogen in the same way as Subset 1.2. Set 2 are 180 μ m thick, \sim 7 Ω cm, phosphorus-doped n-type pyramid textured CZ, (100) silicon wafers. Note that due to the alkaline texturing, the final silicon surface is a (111). Subset 2.1 has a 5 nm thermal oxide on both sides grown in an industrial oxidation furnace at 900 °C. On the basis of Subset 2.1, Subset 2.2 has an additional 60 nm of silicon nitride deposited using Plasma Enhanced Chemical Vapour Deposition (PECVD) on top of the oxide. Figure 2 shows the details of processing of all subsets.

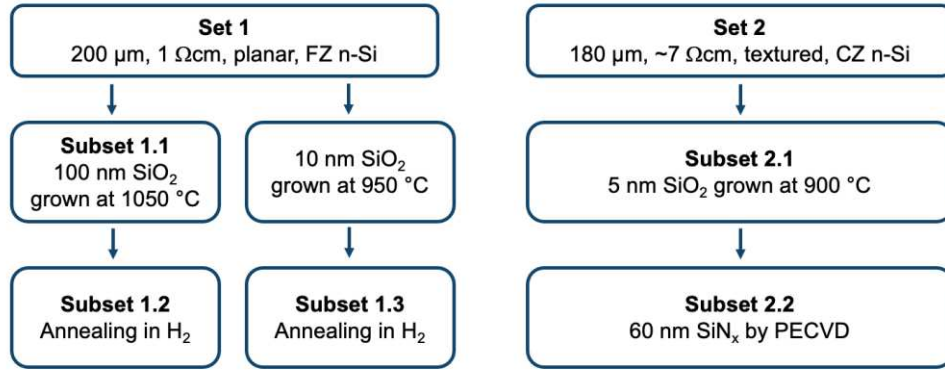


Figure 2. Detailed processing of Set 1 and Set 2 samples.

In order to record changes in the sheet resistance of a sample as a function of surface charge density, we apply corona discharge at 30 kV to the sample surface. This generates an electric field and induces an electron accumulation layer in silicon near the interface. The processing method and the structure of a corona charge-deposited wafer are shown in Figure 3.a. Details on the corona discharge apparatus can be found in [34,35]. For planar Set 1 samples passivated by thermal oxide, Kelvin Probe (KP) measurements were used to acquire the surface potential of the specimen. The charge density was extracted using the formalism in [35], assuming that charge stays at the surface of the dielectric during the measurement period, which has been previously shown to be the case [34]. For textured samples with SiO₂ and SiO₂/SiN_x coatings (Set 2), monitoring the corona ion density using KP is inaccurate as the recorded contact potential difference is influenced by the effective surface area seen by the KP probe. The corona ion density is instead determined by the corona discharge time, with its corresponding charge density calibrated on one planar Set 1 specimen. The Van der Pauw method is used to monitor sheet resistance of a specimen [36]. Ideally, the size of contact should be infinitesimal for accurate measurement. Here we choose a contact size practical for conducting measurements and use a correction factor to compensate the influence of the contact size [37]. The sample structure is shown in Figure 3.b. Details of the Van der Pauw measurement is included in [25]. The sample was first diced into 1 x 1 cm² squares, before the surface dielectric at the corners removed by a diamond scribe. A 100 nm thick aluminium was then deposited for electrical contact at the corners by masked thermal evaporation.

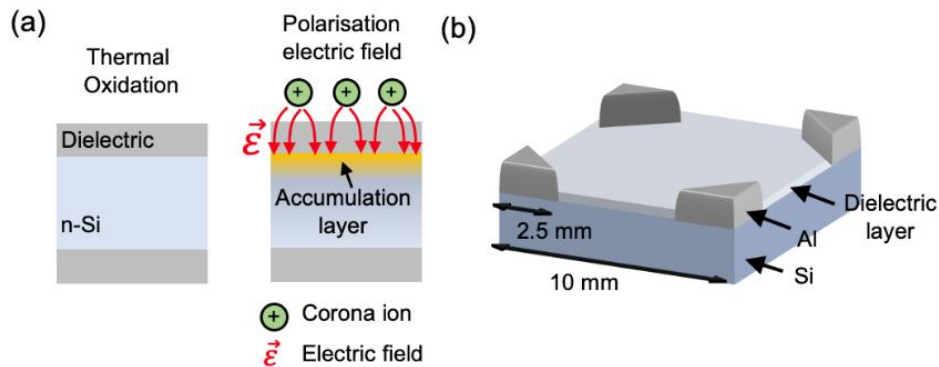


Figure 3. (a) Processing method and schematic of a corona ion-deposited n-Si wafer. (b) Sample structure for Van der Pauw measurement.

3 Impact of Interface States on Space Charge Layer Resistance

Figure 4 shows a schematic energy diagram of an n-Si/SiO₂ interface at an initial neutral state (a), in the presence of charged donor and acceptor interface states (b), and in the presence of dielectric charge (c, d). The conduction and valence bands are flat at the initial neutral state. When donor and acceptor interface states are considered, electrons will occupy the acceptor states below the Fermi level, accompanied by an upward band-bending. In the presence of positive dielectric charge, mirrored

electrons will appear close to the interface in bulk silicon, so that the bands bend downwards, and the Fermi level moves towards the conduction band edge. This will lead to most acceptor states below the Fermi energy being filled with electrons. In the space charge region, charge-induced electrons are free carriers in bulk silicon and contribute to additional wafer conductivity. Since the proportion of trapped electrons is determined by interface state density, wafer sheet resistance can be used as a metric for finding the distribution of interface states near conduction band edge. In the presence of negative dielectric charge, the band near the interface will bend upwards. While increasing negative charge density, the Fermi level will scan across the middle part of the bandgap and then reach the band tail at valence band. This will cause holes to become the dominant carriers, occupying most of the donor states that are above the Fermi level. Hole density in the inversion layer, and therefore inversion layer conductivity, is determined by both the negative dielectric charge density and the amount of charged donor states at the interface. The interface states near valence band edge can be obtained by monitoring inversion layer sheet resistance at controlled negative charge density.

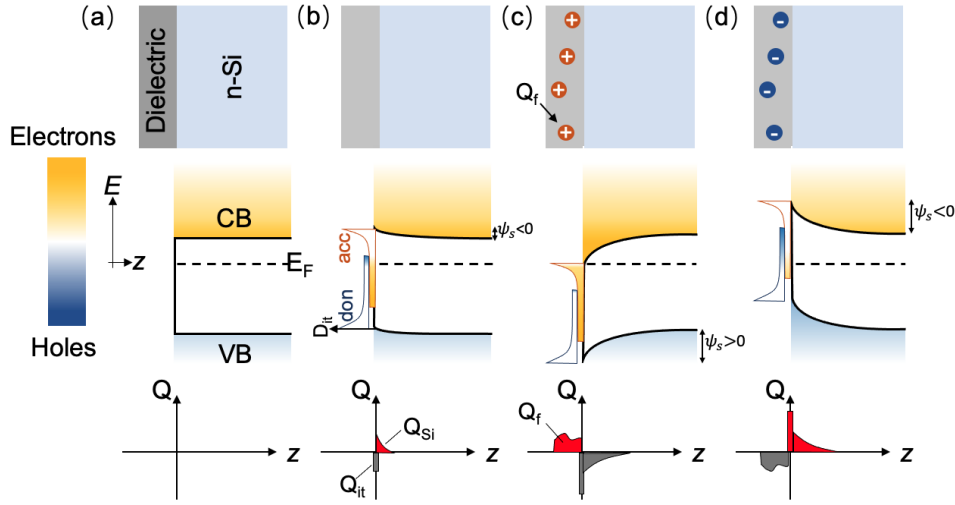


Figure 4. Schematic energy diagram at an n-Si/SiO₂ interface at (a) an ideal neutral state, (b) in the presence of charged donor and acceptor interface states, and in the presence of (c) positive or (d) negative dielectric charge. Redrawn from [38].

A model was developed in Sentaurus TCAD [39] to better understand the Si/SiO₂ interface, which accounts for all physical phenomena involved in the formation of the space charge layer. The model comprises a 200 μm thick, 1 Ωcm n-Si wafer, with an oxide passivation layer on both sides. Positive dielectric charge was defined at the front Si/SiO₂ interface. The interface was defined following the common parametrisation as reported in [40], with interface state densities at midgap and band tails as primary parameters. The interface defect density profile near both band edges follows an exponential dependency on energy, as shown in equations (1) and (2):

$$D_{it}(CB, acceptor) = D_{it}(max, CB, acceptor) \times e^{\frac{(1.1-E)}{E_{CB,trap}}} \quad (1)$$

$$D_{it}(VB, donor) = D_{it}(max, VB, donor) \times e^{-\frac{E}{E_{VB,trap}}} \quad (2)$$

where $D_{it}(CB, acceptor)$ and $D_{it}(VB, donor)$ describe the acceptor/donor band-tail interface state density. $D_{it}(max, CB, acceptor)$ and $D_{it}(max, VB, donor)$ are the maximum interface state density at conduction/valence band edge, and E is the energy of the states from valence band edge in eV. $E_{CB,trap}$ and $E_{VB,trap}$ represent the slope of the tail, indicating its dependence on energy. Here $E_{CB,trap}$ has been set to 0.02 eV and $E_{VB,trap}$ to 0.024 eV to reflect average values extracted from previous works [11,17,20]. Since the energy slope and maximum states of the band tails may vary at different silicon/dielectric interfaces [41], we integrate all tail interface states into a single metric N_{it} (acceptor/donor) that describes the total amount of tail interface states available for occupation. To allow fast fitting we only vary the maximum interface state density at band edge $D_{it}(max)$, while maintaining the tail slopes, $E_{CB,trap}$ and $E_{VB,trap}$, constant. As an example, Figure 5 shows the D_{it} distribution at Si/SiO₂ interface in a model with D_{it} (midgap) being $10^{11} \text{ eV}^{-1}\text{cm}^{-2}$,

$D_{it}(max, CB, acceptor) = 10^{14} \text{ eV}^{-1}\text{cm}^{-2}$, and $D_{it}(max, VB, donor) = 10^{14} \text{ eV}^{-1}\text{cm}^{-2}$. We calculate the N_{it} (acceptor/donor) as the area under the tail, corresponding to the maximum state occupation the tail can take. N_{it} (acceptor/donor) comprehensively accounts for both the tail maximum value and its slope. In this work we will report the N_{it} (acceptor/donor) as the primary metric for characterising the impact of the tail state concentrations. The Inversion and Accumulation Layer Mobility Model (IALMob) reported for simulation of MOSFETs was used here to model the mobility throughout the sample bulk and in the space charge layer [42,43]. A density gradient quantum-mechanical model was used to account for the confined carrier distributions occurring near semiconductor–insulator interfaces [44,45]. Including these carrier density and mobility effect is critical to achieve a model that correctly reflected the measurements. The equilibrium state was then simulated, and the carrier density and mobility were extracted as a function of the distance from the Si/SiO₂ interface. Figure 6 shows the extracted carrier density and mobility from a simulation with positive charge density of $9 \times 10^{12} \text{ cm}^{-2}$ at the front dielectric. These were then integrated over the entire sample depth to calculate the wafer sheet resistance, following equation (3):

$$R_S(wafer) = \frac{1}{\int_0^{thickness} (nq\mu_n + pq\mu_p) dt} \quad (3)$$

where n and p are electron/hole density, μ_n and μ_p are electron/hole mobility, and q is the elementary charge.

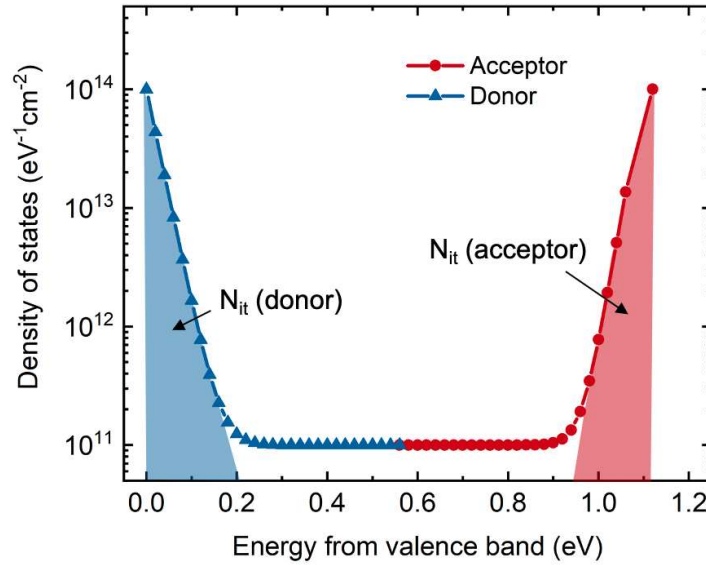


Figure 5. Density of states distribution at Si/SiO₂ interface in a model with D_{it} being 10^{11} , 10^{14} , and $10^{14} \text{ eV}^{-1}\text{cm}^{-2}$ at midgap, conduction band edge, and valence band edge.

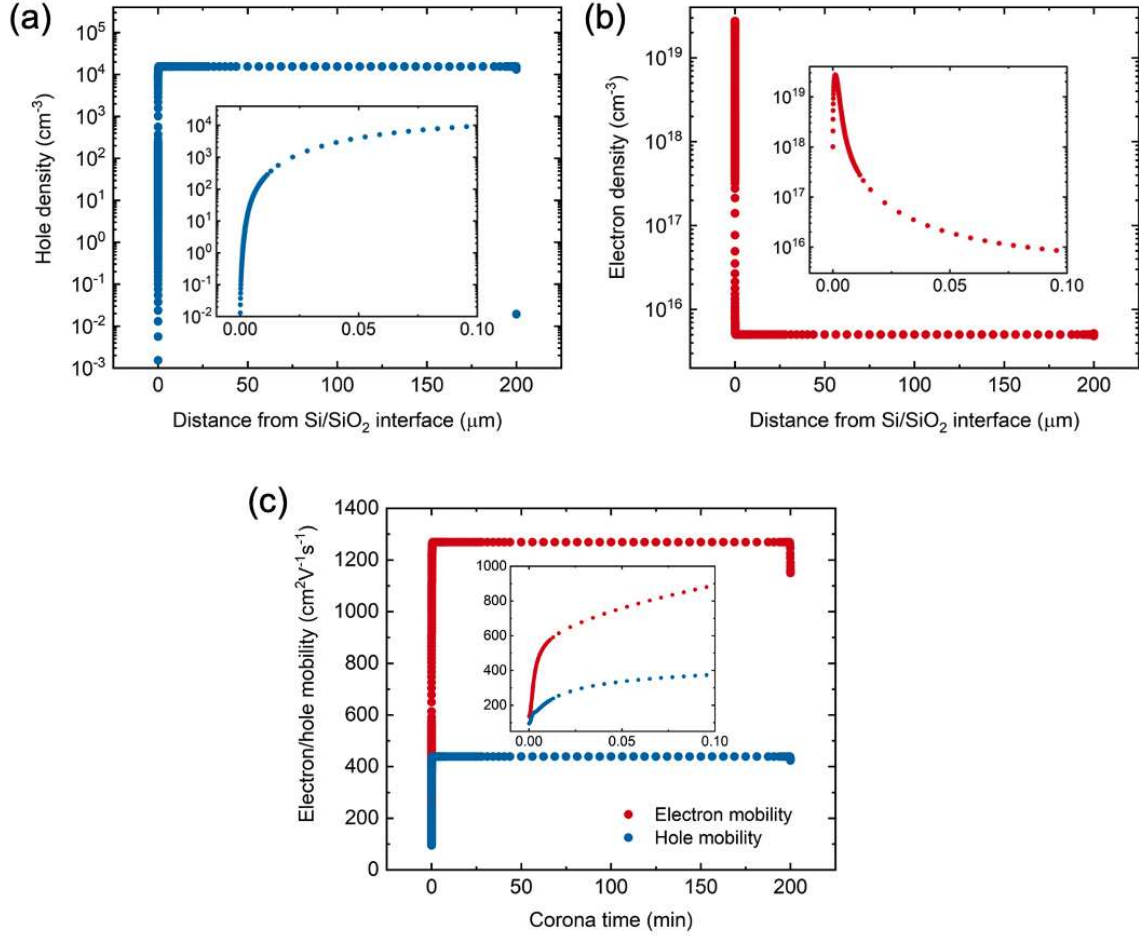


Figure 6. Simulated carrier density including (a) electrons and (b) holes. (c) Carrier mobility across the whole wafer extracted from a n-type, 1 Ωcm model with positive charge density of $9 \times 10^{12} \text{ cm}^{-2}$ at the front dielectric. D_{it} is 10^{11} , 10^{14} , and $10^{14} \text{ eV}^{-1} \text{ cm}^{-2}$ at midgap, conduction band edge, and valence band edge in the model.

As represented in the energy diagram in Figure 4, increasing the positive charge density will cause the Fermi level to scan across first the middle part of the bandgap, and then the band tail at conduction band edge. Wafer sheet resistance as a function of positive charge density was simulated to reflect the response of the space charge layer while introducing positive charge at the front dielectric. Since interface states at midgap and band tails can host field-induced electrons, the wafer sheet resistance vs. charge density curve was simulated for a range of D_{it} at both midgap and conduction band edge. We simulate a charge concentration up to $9 \times 10^{12} \text{ q/cm}^2$, which approaches the practical limit of gate breakdown field in most thin film materials [46,47]. Figure 7 shows wafer sheet resistance vs. positive charge density curves simulated from a 200 μm thick, 1 Ωcm n-Si substrate. For Figure 7.a, the maximum D_{it} at conduction band edge is $10^{14} \text{ eV}^{-1} \text{ cm}^{-2}$, and varied D_{it} (midgap) is applied. For Figure 7.b, D_{it} (midgap) is $10^{11} \text{ eV}^{-1} \text{ cm}^{-2}$, and N_{it} (acceptor) near the conduction band edge is varied. In Figure 7.a, the change in wafer sheet resistance is less than 0.1 Ω/sq for D_{it} (midgap) below $10^{12} \text{ eV}^{-1} \text{ cm}^{-2}$. Since this is the case for most passivated wafers [1,48], it is concluded that the variation of D_{it} (midgap) has a minor effect on local carrier distribution, and therefore on the conductivity of the space charge layer. This was expected as described in Section 1. The effect of the number of acceptor tail states, N_{it} (acceptor), is depicted in Figure 7.b. Here it is evident that there are large changes in (i) wafer sheet resistance and (ii) the dependence of resistance on positive surface charge density. The wafer sheet resistance vs. positive charge density curve is therefore useful for determining the distribution of interface states, especially for those near the conduction band edge.

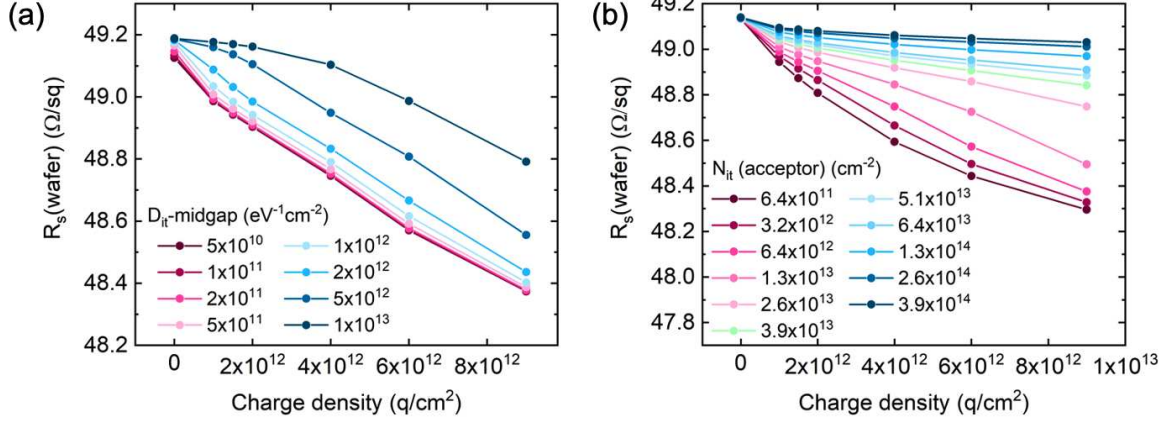


Figure 7. Simulated wafer sheet resistance vs. positive charge density curves of a 200 μm thick, 1 Ωcm n-Si substrate at various (a) D_{it} (midgap), and (b) N_{it} (acceptor) near conduction band edge.

We also evaluate the potential of the method to detect the amount of donor tail states near valence band edge, N_{it} (donor). An inversion layer sheet resistance as a function of negative charge density was simulated from the same 200 μm thick, 1 Ωcm n-Si substrate. Figure 8 shows the inversion layer sheet resistance vs. negative charge density with varied N_{it} (donor), for charge concentrations up to $9 \times 10^{12} \text{ cm}^{-2}$. D_{it} (midgap) is set to $10^{11} \text{ eV}^{-1}\text{cm}^{-2}$. The thickness of the inversion layer is determined by where the electron density exceeds that of holes. The effect of N_{it} (donor) is shown in Figure 8. Similar to the effect of N_{it} (acceptor) in Figure 7.b, large changes are observed in (i) inversion layer sheet resistance, and (ii) the dependence of resistance on negative surface charge density. The parameters used to describe the model are listed in Table 1. Based on the analysis above, measurements of R_s in combination with simulations make it possible to detect both the acceptor and donor tail states.

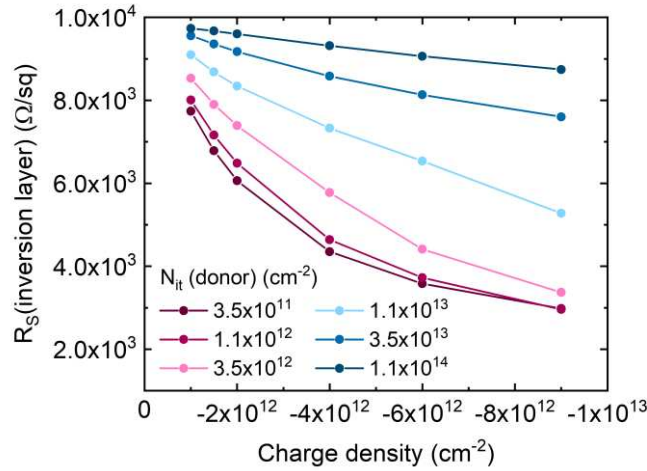


Figure 8. Simulated inversion layer sheet resistance vs. negative charge density of a 200 μm thick, 1 Ωcm n-Si substrate at various N_{it} (donor) near valence band edge.

Table 1. Summary of parameters used for simulation of wafer sheet resistance in the presence of dielectric charge in Sentaurus TCAD.

Parameter	Value
Wafer thickness	200 μm
Bulk base resistivity	n-type, 0.96-1.04 Ωcm
SRH bulk lifetime	$\tau_n = 0.371 \text{ ms}$, $\tau_p = 3.71 \text{ ms}$
Dielectric charge density	$-9 \times 10^{12} - 9 \times 10^{12} \text{ cm}^{-2}$
D_{it} (midgap)	$5 \times 10^{10} - 10^{13} \text{ eV}^{-1}\text{cm}^{-2}$

4 Method for Extraction of Interface Properties

We developed a method to extract N_{it} (acceptor) of an n-type specimen from a combination of measurements and simulation. First, we acquire a wafer sheet resistance vs. positive charge density curve of a passivated silicon wafer by recording the wafer sheet resistance while introducing controlled amounts of positive corona charges to the sample surface. A series of wafer sheet resistance vs. positive charge density curves are then generated by simulations with fine adjustments of wafer resistivity and N_{it} (acceptor) to fit the experimental curve. The combination of wafer resistivity and N_{it} (acceptor) generating the best fitting curve are extracted for the specimen. Examples of N_{it} (acceptor) extraction are given in Section 5.

Fitting between the simulated and experimental data is determined by two metrics: (i) the wafer sheet resistance, which can shift the curve in the y-axis, and (ii) the slope of the curve at high charge densities ($2 - 9 \times 10^{12} \text{ cm}^{-2}$), which reflects the dependence of wafer sheet resistance on positive charge density. The reliability of this method is evaluated here by calculating the slope of the $2 - 9 \times 10^{12} \text{ cm}^{-2}$ range of the curve as a function of N_{it} (acceptor). Figure 9 shows the curves extracted from simulations on a 200 μm thick, 1 Ωcm n-Si substrate. In Figure 9.a, D_{it} (midgap) is $10^{11} \text{ eV}^{-1} \text{ cm}^{-2}$ and N_{it} (donor) is $3.54 \times 10^{12} \text{ cm}^{-2}$. Figure 9.a shows the change in slope as a function of N_{it} (acceptor), with the slope being more sensitive at lower N_{it} (acceptor). For N_{it} (acceptor) below $10^{13} \text{ eV}^{-1} \text{ cm}^{-2}$, the amount of interface states to accommodate the induced electrons is too low to be differentiated by monitoring wafer sheet resistance. This method is therefore not applicable for N_{it} (acceptor) below $10^{13} \text{ eV}^{-1} \text{ cm}^{-2}$. Wafer resistivity is also varied to show its effect on the simulated dependence. Here it is clear that a change of wafer resistivity by 0.04 Ωcm will cause an evident shift of the curve, meaning that the wafer resistivity has to be precise in the model for an accurate extraction of N_{it} (acceptor). Since the non-uniformity in wafer resistivity is unavoidable even across a same wafer, along with the slope, the simulated and experimental R_s -Q relations require fitting in y-axis for correct base resistance, and subsequent extraction of N_{it} (acceptor). D_{it} (midgap) is varied in Figure 9.b where it is clear that it has almost no effect on the curve. Therefore, interface states at midgap does not affect extraction of N_{it} (acceptor) with this method. According to the analysis above, N_{it} (acceptor) can be extracted with this method with no evident artifacts originating from wafer resistivity variations, or variation in D_{it} (midgap).

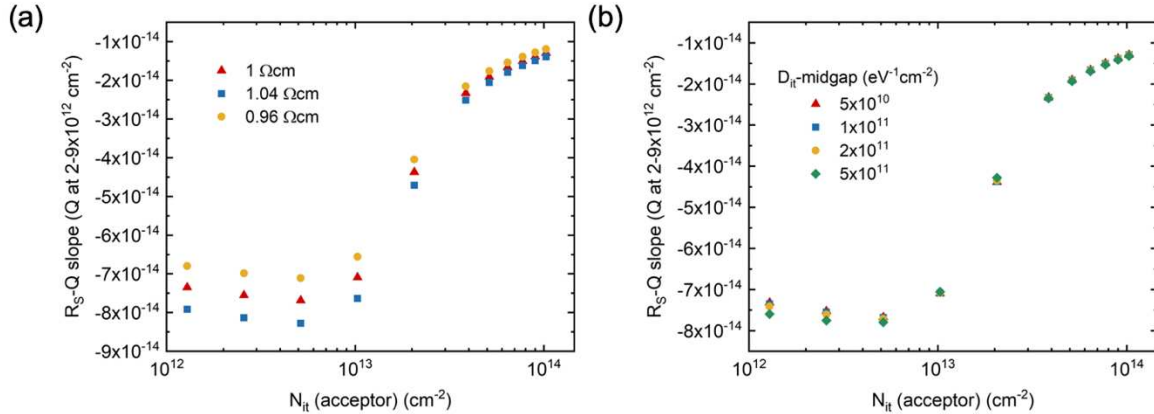


Figure 9. Slope of simulated wafer sheet resistance vs. positive charge density curve on a 200 μm thick, 1 Ωcm n-Si substrate at charge density in the range of $2 - 9 \times 10^{12} \text{ cm}^{-2}$, as a function of N_{it} (acceptor), with varied (a) wafer resistivity, and (b) D_{it} (midgap).

To extract N_{it} (donor), we need to measure sheet resistance of an inversion layer. It is to note that inversion layer could not be contacted using the sample structure in Figure 3.b. This is because of the discontinuity in inversion layer underneath the Aluminium patches, which can be solved by local doping. Due to the lack of local doping tools in our laboratory, the method to extract N_{it} (donor) is not evaluated in this work.

5 Extraction of Interface Properties

The amount of acceptor band-tail states of Set 1 and Set 2 samples is extracted to demonstrate the potential of this characterisation method. For Set 1 samples, wafer sheet resistance was recorded as shown in the square and circle symbols in Figure 10.a. Wafer resistivity and N_{it} (acceptor) at the Si/SiO₂ interface were then adjusted in the numerical model. Wafer sheet resistance as a function of positive charge density are shown in Figure 10.a. The best fit for each sample is shown as a solid line, and the parameters obtained are listed in Table 2. The extracted N_{it} (acceptor) values for each subset from Set 1 are compared in Figure 10.b, and are found in agreement with data reported in [11,17,20,38]. It is to note that the N_{it} (acceptor) reported for the 100 nm oxide subsets are at the lower end of the detection limit observed in Figure 9. When extracting the R_s - Q_f slope from the experimental data, the model would seem to require lower N_{it} (acceptor) to fit the slope more accurately. This condition appears to be due to the mobility model chosen here (IALMob). This model has been mainly tested in MOSFETs that use base dopant density of the order of $>10^{16} \text{ cm}^{-3}$ [42,43], while a typical dopant density in this work is $5 \times 10^{15} \text{ cm}^{-3}$. Better accuracy in extracting N_{it} (acceptor) would hence require a tested model of accumulation and inversion layer carrier mobility for dopant densities commonly used in PV devices. In Figure 10.b, no evident drop in N_{it} (acceptor) is observed for the Si/SiO₂ (100 nm) sample after an FGA, indicating that the enhanced chemical passivation by FGA is not evident at the band tail. For the two subsets with FGA, the subset with 10 nm of oxide presents a lower N_{it} (acceptor) than the one with 100 nm of oxide, which may originate from the difference in oxidation temperature (1050 °C for 100 nm vs. 950 °C for 10 nm specimens).

Set 2 samples are textured wafers with SiO₂ and SiO₂/SiN_x coatings. In this case the corona charge density is determined by the time of corona discharge. The corresponding charge density is pre-calibrated, as is described in Section 2. The calibration is included in the supplementary material. SiN_x thin films are known to contain fixed positive charge. Since the electron accumulation layer is induced by the charge in the SiN_x plus that added via corona discharge, the amount of charge initially present in SiN_x is required to determine the net charge density. The typical charge density of a SiO₂ coating is about 10^{11} cm^{-2} [49–52], which is negligible compared with the corona charge density, and is therefore not considered in this work. Figure 10.e shows wafer sheet resistance as a function of negative charge density for the two textured silicon subsets. While adding negative corona charge, the fixed positive charge at the dielectric will be compensated, cancelling the electron accumulation layer, before depleting and inverting it into p-type at higher negative charge density. The sample structure for Van der Pauw measurements has aluminium regions in contact with n-type silicon, where the carrier distribution is not affected by corona charge or charge in the SiN_x. Since the contacts are made to n-type Si, fewer charge flow though the depleted and then inverted (p-type) region underneath the dielectric. Therefore, increasing the negative corona charge results in an increase in the measured wafer sheet resistance, before a plateau is reached at the transition from depletion to inversion. By aligning the transition of the two subsets in Figure 10.e, we can determine the extra dielectric charge from SiN_x, which is characterised to be $\sim 1.2 \times 10^{12} \text{ cm}^{-2}$. This is in good agreement with data reported in [38]. The experimental wafer sheet resistance of Set 2 samples as a function of net charge density is shown in Figure 10.c. The recorded R_s plateaued at charge densities exceeding 10^{13} cm^{-2} , likely as a result of the finite breakdown of the dielectric stack. The net charge density does not increase when breakdown occurs, as it has been found in previous work [47,53]. N_{it} (acceptor) and wafer resistivity were adjusted in the simulation to fit the experimental data in the range of charge $<10^{13} \text{ cm}^{-2}$. $E_{CB,trap}$ was adjusted to 0.022 eV in this model to reflect the fact that the (111) surface has more defect states than (100) surfaces in Set 1. The solid lines represent the best fit simulated curves. The fittings are again affected by the non-ideal mobility model. The interface parameters extracted for each sample are shown in Table 3. A significant drop in N_{it} (acceptor) is observed due to the 60 nm of SiN_x deposition on top of the Si/SiO₂ (5 nm) structure. This indicates enhanced surface passivation at band tails as a product of the PECVD nitride. While we present the extraction of N_{it} (acceptor) from n-type Si, the technique can be used for N_{it} (donor) detection provided that an electrical contact to the inversion layer can be produced. The same applies to a p-type sample.

Overall, these results clearly corroborate the fact that interface states not only act as recombination centres for photo-generated carriers, but also accommodate charge and affect local carrier density. Interface states are therefore important for surface architectures based on band bending, for example, field-effect passivation, inversion layer cells, MOSFETs, and field-induced photodiodes. The characterisation technique studied in this work is shown to allow sensitive detection of interface states at band tails and is therefore of importance across various interfaces in optoelectronic devices.

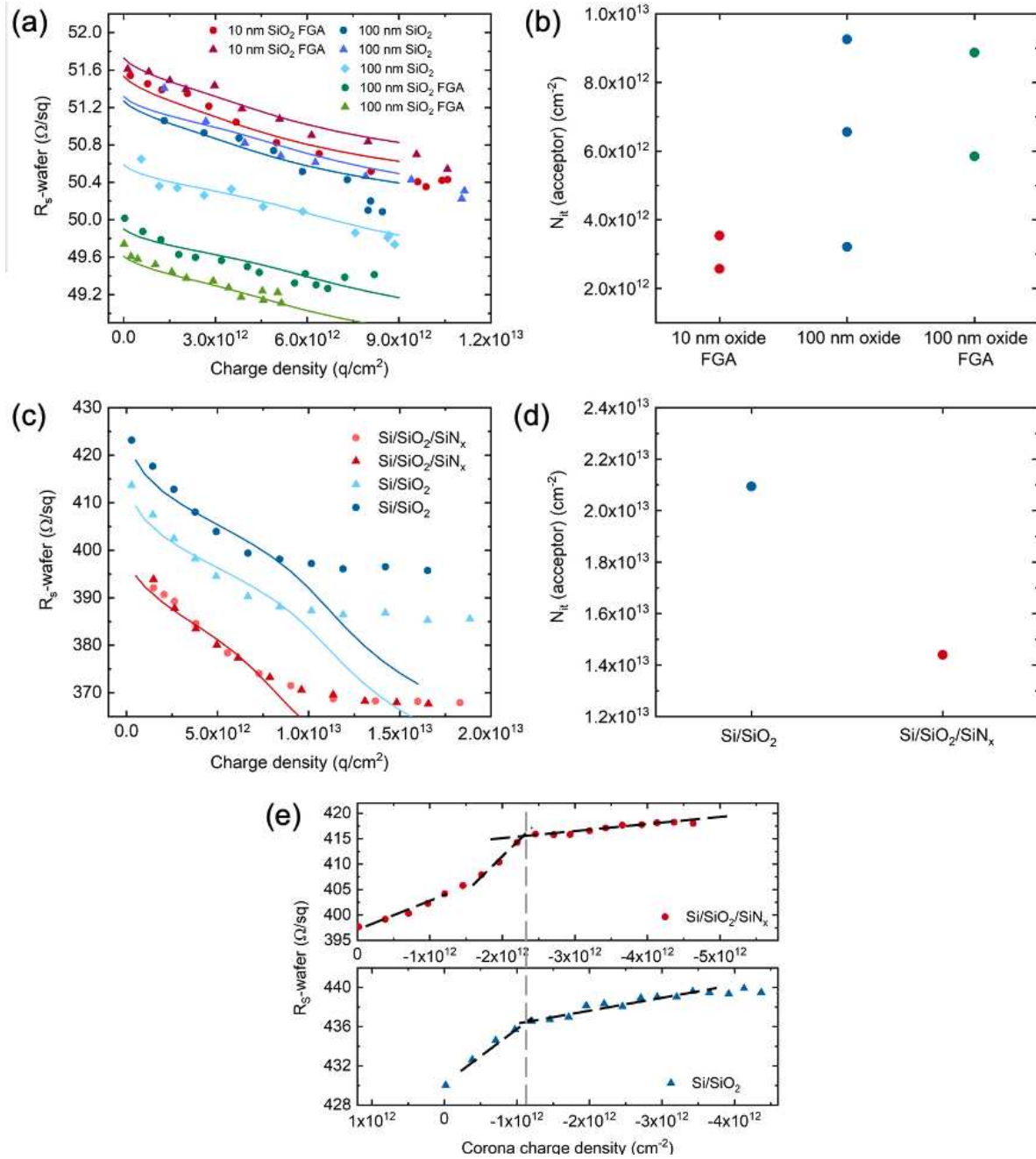


Figure 10. (a) Experimental (symbols) and simulated (lines) wafer sheet resistance vs. positive charge density curves, and (b) extracted N_{it} (acceptor) for Set 1 samples. (c) Experimental and simulated wafer sheet resistance vs. positive charge density curves, and (d) extracted N_{it} (acceptor) for Set 2 samples. (e) Wafer sheet resistance vs. negative charge density curves of Set 2 samples.

Table 2. Details of parameters used in simulations for best fits with experimental wafer sheet resistance vs. charge density curves of Set 1 samples.

	10 nm oxide, FGA		100 nm oxide			100 nm oxide, FGA	
	Sample 1	Sample 2	Sample 1	Sample 2	Sample 3	Sample 1	Sample 2
Wafer resistivity	1.053	1.049	1.045	1.044	1.03	1.016	1.01

D_{it} (max, CB, acceptor)	5.5×10^{13}	4×10^{13}	1.02×10^{14}	5×10^{13}	1.44×10^{14}	1.38×10^{14}	9.1×10^{13}
N_{it} (acceptor)	3.54×10^{12}	$< 2.57 \times 10^{12}$	6.56×10^{12}	$< 3.21 \times 10^{12}$	9.26×10^{12}	8.87×10^{12}	5.85×10^{12}

Table 3. Details of parameters used in simulations for best fits with experimental wafer sheet resistance vs. charge density curves of Set 2 samples.

	Si/SiO₂		Si/SiO₂/SiN_x	
	Sample 1	Sample 2	Sample 1	Sample 2
Wafer resistivity	8.65	8.45	8.2	
D_{it} (max, CB, acceptor)	3.2×10^{14}		2.2×10^{14}	
N_{it} (acceptor)	2.09×10^{13}		1.44×10^{13}	

6 Conclusions

At a semiconductor-dielectric system, the concentration of charge-induced carriers and therefore conductivity of the induced layer is dependent on dielectric charge density and interface state density. This work explores the potential to extract interface state density near both band edges from measurements of induced layer conductivity at controlled charge density with the aid of simulations. Simulations of wafer sheet resistance vs. positive charge density showed changes in D_{it} (midgap) at the n-Si/SiO₂ interface have a minor effect on the carrier densities at the interface. On the other hand, changes in N_{it} (acceptor) cause a remarkable shift in both the wafer sheet resistance and the dependence of wafer sheet resistance to surface charge density. Such feature was found key in extracting the N_{it} (acceptor) from measurements. Similar effects were observed for N_{it} (donor) via simulating inversion layer sheet resistance in the presence of negative charge, showing the possibility of extracting both N_{it} (acceptor) and N_{it} (donor) with this method. The sensitive detection of N_{it} (acceptor), and potentially that of N_{it} (donor) makes this method a powerful complement to current interface characterisation techniques. The technique can therefore provide insight in understanding and manipulating of carrier distribution at semiconductor–dielectric interfaces, and point to strategies for improvement.

7 Supplementary Materials

A calibration of positive and negative corona charge density at various corona discharge time at 30 kV is included in the online supplementary materials. All experimental data published in this article can be downloaded from <http://ora.ox.ac.uk>.

8 Acknowledgements

All authors are thankful to Radka Chakalova for assistance in cleanroom processing. M. Yu would like to thank the China Scholarship Council for funding her doctoral studies. P.P. Altermatt acknowledge support from Black Silicon Photovoltaics grant EP/R005303/1. R. S. Bonilla was supported by the Royal Academy of Engineering under the Research Fellowship scheme and acknowledges the support from the EPSRC Postdoctoral Fellowship EP/ M022196/1.

9 References

- [1] A.G. Aberle, Crystalline silicon solar cells : advanced surface passivation and analysis, Centre for Photovoltaic Engineering, University of New South Wales, Sydney, 2009.
- [2] J.F. Wager, K. Kuhn, Device Physics Modeling of Surfaces and Interfaces from an Induced Gap State Perspective, Crit. Rev. Solid State Mater. Sci. 42 (2017) 373–415. <https://doi.org/10.1080/10408436.2016.1223013>.

- [3] J. Robertson, Band offsets of wide-band-gap oxides and implications for future electronic devices, *J. Vac. Sci. & Technol. B Microelectron. Nanom. Struct. Process. Meas. Phenom.* 18 (2000) 1785–1791. <https://doi.org/10.1116/1.591472>.
- [4] C. Freysoldt, B. Grabowski, T. Hickel, J. Neugebauer, G. Kresse, A. Janotti, C.G. de Walle, First-principles calculations for point defects in solids, *Rev. Mod. Phys.* 86 (2014) 253–305. <https://doi.org/10.1103/RevModPhys.86.253>.
- [5] H. Feichtinger, Deep Centers in Semiconductors, in: *Handb. Semicond. Technol.*, John Wiley & Sons, Ltd, 2000: pp. 167–229. <https://doi.org/10.1002/9783527621842.ch4>.
- [6] V. Heine, Theory of Surface States, *Phys. Rev.* 138 (1965) A1689–A1696. <https://doi.org/10.1103/PhysRev.138.A1689>.
- [7] J. Tersoff, Schottky Barrier Heights and the Continuum of Gap States, *Phys. Rev. Lett.* 52 (1984) 465–468. <https://doi.org/10.1103/PhysRevLett.52.465>.
- [8] T. Iffländer, S. Rolf-Pissarczyk, L. Winking, R.G. Ulbrich, A. Al-Zubi, S. Blügel, M. Wenderoth, Local Density of States at Metal-Semiconductor Interfaces: An Atomic Scale Study, *Phys. Rev. Lett.* 114 (2015) 146804. <https://doi.org/10.1103/PhysRevLett.114.146804>.
- [9] F. Giustino, A. Pasquarello, Electronic and dielectric properties of a suboxide interlayer at the silicon–oxide interface in MOS devices, *Surf. Sci.* 586 (2005) 183–191. <https://doi.org/10.1016/j.susc.2005.05.012>.
- [10] S. Markov, P. Sushko, C. Fiegna, E. Sangiorgi, A. Shluger, A. Asenov, From ab initio properties of the Si-SiO₂ interface, to electrical characteristics of metal-oxide-semiconductor devices, *J. Phys. Conf. Ser.* 242 (2010) 12010. <https://doi.org/10.1088/1742-6596/242/1/012010>.
- [11] H. Flietner, W. Füssel, N.D. Sinh, H. Angermann, Density of states and relaxation spectra of etched, H-terminated and naturally oxidized Si-surfaces and the accompanied defects, *Appl. Surf. Sci.* 104–105 (1996) 342–348. [https://doi.org/10.1016/S0169-4332\(96\)00168-7](https://doi.org/10.1016/S0169-4332(96)00168-7).
- [12] W. Shockley, W.T. Read, Statistics of the Recombinations of Holes and Electrons, *Phys. Rev.* 87 (1952) 835–842. <https://doi.org/10.1103/PhysRev.87.835>.
- [13] R.N. Hall, Electron-Hole Recombination in Germanium, *Phys. Rev.* 87 (1952) 387. <https://doi.org/10.1103/PhysRev.87.387>.
- [14] R.S. Bonilla, B. Hoex, P. Hamer, P.R. Wilshaw, Dielectric surface passivation for silicon solar cells: A review, *Phys. Status Solidi Appl. Mater. Sci.* 214 (2017) 1–30. <https://doi.org/10.1002/pssa.201700293>.
- [15] J. Schmidt, R. Peibst, R. Brendel, Surface passivation of crystalline silicon solar cells: Present and future, *Sol. Energy Mater. Sol. Cells.* 187 (2018) 39–54. <https://doi.org/10.1016/j.solmat.2018.06.047>.
- [16] S.W. Glunz, F. Feldmann, SiO₂ surface passivation layers – a key technology for silicon solar cells, *Sol. Energy Mater. Sol. Cells.* 185 (2018) 260–269. <https://doi.org/10.1016/j.solmat.2018.04.029>.
- [17] H. Flietner, U-Shaped Distributions at Semiconductor Interfaces and the Nature of the Related Defect Centres, *Phys. Status Solidi.* 91 (1985) 153–164. <https://doi.org/10.1002/pssa.2210910120>.
- [18] Y.W. Lam, E.H. Rhoderick, Surface-state density and surface potential in MIS capacitors by surface photovoltage measurements. II, *J. Phys. D. Appl. Phys.* 4 (1971) 1376–1389. <https://doi.org/10.1088/0022-3727/4/9/319>.
- [19] H. Flietner, Spectrum and nature of defects at interfaces of semiconductors with predominant homopolar bonding, *Surf. Sci.* 200 (1988) 463–471. [https://doi.org/10.1016/0039-6028\(88\)90553-5](https://doi.org/10.1016/0039-6028(88)90553-5).
- [20] W. Füssel, M. Schmidt, H. Angermann, G. Mende, H. Flietner, Defects at the Si/SiO₂ interface: Their nature and behaviour in technological processes and stress, *Nucl. Instruments Methods Phys. Res. Sect. A Accel. Spectrometers, Detect. Assoc. Equip.* 377 (1996) 177–183. [https://doi.org/10.1016/0168-9002\(96\)00205-7](https://doi.org/10.1016/0168-9002(96)00205-7).
- [21] M.H. Cohen, M.Y. Chou, E.N. Economou, S. John, C.M. Soukoulis, Band Tails, Path Integrals,

- Instantons, Polarons, and All That, IBM J. Res. Dev. 32 (1988) 82–92. <https://doi.org/10.1147/rd.321.0082>.
- [22] S.W. Glunz, D. Biro, S. Rein, W. Warta, Field-effect passivation of the SiO₂-Si interface, J. Appl. Phys. 86 (1999) 683–691. <https://doi.org/10.1063/1.370784>.
- [23] K.R. McIntosh, S.C. Baker-Finch, N.E. Grant, A.F. Thomson, S. Singh, I.D. Baikie, Charge Density in Atmospheric Pressure Chemical Vapor Deposition TiO₂ on SiO₂-Passivated Silicon, J. Electrochem. Soc. 156 (2009) G190. <https://doi.org/10.1149/1.3216029>.
- [24] R.S. Bonilla, K. Collett, L. Rands, G. Martins, R. Lobo, P.R. Wilshaw, Stable, Extrinsic, Field Effect Passivation for Back Contact Silicon Solar Cells, Solid State Phenom. 242 (2015) 67–72. <https://doi.org/10.4028/www.scientific.net/SSP.242.67>.
- [25] M. Yu, Y. Shi, J. Deru, I. Al-Dhahir, S. McNab, D. Chen, M. Voss, E.-T. Hwu, A. Ciesla, B. Hallam, P. Hamer, P.P. Altermatt, P. Wilshaw, R.S. Bonilla, Assessing the Potential of Inversion Layer Solar Cells Based on Highly Charged Dielectric Nanolayers, Phys. Status Solidi – Rapid Res. Lett. n/a (2021). <https://doi.org/https://doi.org/10.1002/pssr.202100129>.
- [26] F. Werner, J. Schmidt, Manipulating the negative fixed charge density at the c-Si/Al₂O₃ interface, Appl. Phys. Lett. 104 (2014). <https://doi.org/10.1063/1.4867652>.
- [27] R. Har-Lavan, D. Cahen, 40 years of inversion layer solar cells: From MOS to conducting polymer/inorganic hybrids, IEEE J. Photovoltaics. 3 (2013) 1443–1459. <https://doi.org/10.1109/JPHOTOV.2013.2270347>.
- [28] J.J. Liou, A. Ortiz-Conde, F. Garcia-Sanchez, MOSFET physics and modeling, in: Anal. Des. Mosfets Model. Simul. Param. Extr., Springer US, Boston, MA, 1998: pp. 1–108. https://doi.org/10.1007/978-1-4615-5415-8_1.
- [29] M.A. Juntunen, J. Heinonen, V. Vähänissi, P. Repo, D. Valluru, H. Savin, Near-unity quantum efficiency of broadband black silicon photodiodes with an induced junction, Nat. Photonics. 10 (2016) 777–781. <https://doi.org/10.1038/nphoton.2016.226>.
- [30] C. N. Berglund, Surface States at Steam-Grown Silicon-Silicon Dioxide Interfaces, IEEE Trans. Ele. ED-13 (1966) 701–705. <https://doi.org/10.1080/10408437308245838>.
- [31] C.R. Helms, E.H. Poindexter, The silicon-silicon dioxide system: Its microstructure and imperfections, Reports Prog. Phys. 57 (1994) 791–852. <https://doi.org/10.1088/0034-4885/57/8/002>.
- [32] D. Jousse, J. Kanicki, J.H. Stathis, Observation of multiple silicon dangling bond configurations in silicon nitride, Appl. Phys. Lett. 54 (1989) 1043–1045. <https://doi.org/10.1063/1.101558>.
- [33] Z. Xin, S. Duttagupta, M. Tang, Z. Qiu, B. Liao, A.G. Aberle, R. Stangl, An Improved Methodology for Extracting the Interface Defect Density of Passivated Silicon Solar Cells, IEEE J. Photovoltaics. 6 (2016) 1080–1089. <https://doi.org/10.1109/JPHOTOV.2016.2576685>.
- [34] R.S. Bonilla, C. Reichel, M. Hermle, P. Hamer, P.R.P.R. Wilshaw, Long term stability of c-Si surface passivation using corona charged SiO₂, Appl. Surf. Sci. 412 (2017) 657–667. <https://doi.org/10.1016/j.apsusc.2017.03.204>.
- [35] R.S. Bonilla, N. Jennison, D. Clayton-Warwick, K.A. Collett, L. Rands, P.R. Wilshaw, Corona Charge in SiO₂: Kinetics and Surface Passivation for High Efficiency Silicon Solar Cells, Energy Procedia. 92 (2016) 326–335. <https://doi.org/10.1016/j.egypro.2016.07.090>.
- [36] L.J. van der Pauw, A Method of Measuring Specific Resistivity and Hall Effect of Discs of Arbitrary Shape, Philips Res. Reports. 13 (1958) 1–9.
- [37] R. Chwang, B.J. Smith, C.R. Crowell, Contact size effects on the van der Pauw method for resistivity and Hall coefficient measurement, Solid State Electron. 17 (1974) 1217–1227. [https://doi.org/10.1016/0038-1101\(74\)90001-X](https://doi.org/10.1016/0038-1101(74)90001-X).
- [38] R.S. Bonilla, I. Al-dhahir, M. Yu, P. Hamer, P.P. Altermatt, Charge fluctuations at the Si – SiO₂ interface and its effect on surface recombination in solar cells, Sol. Energy Mater. Sol. Cells. 215 (2020) 110649. <https://doi.org/10.1016/j.solmat.2020.110649>.
- [39] Synopsys, Sentaurus Device, (n.d.). <https://www.synopsys.com/silicon/tcad/device-simulation/sentaurus-device.html> (accessed April 29, 2021).

- [40] S.W. Glunz, S. Rein, J. Knobloch, W. Wettling, T. Abe, Comparison of boron- and gallium-doped p-type Czochralski silicon for photovoltaic application, *Prog. Photovoltaics Res. Appl.* 7 (1999) 463–469. [https://doi.org/10.1002/\(SICI\)1099-159X\(199911/12\)7:6<463::AID-PIP293>3.0.CO;2-H](https://doi.org/10.1002/(SICI)1099-159X(199911/12)7:6<463::AID-PIP293>3.0.CO;2-H).
- [41] R.A. Street, Hydrogenated Amorphous Silicon, 1991. <https://doi.org/10.1017/cbo9780511525247>.
- [42] Syed Aon Mujtaba, Advanced Mobility Models for Design and Simulation of Deep Submicrometer Mosfets, Thesis. (1995).
- [43] M.N. Darwish, J.L. Lentz, M.R. Pinto, P.M. Zeitzoff, T.J. Krutsick, H.H. Vuong, An improved electron and hole mobility model for general purpose device simulation, *IEEE Trans. Electron Devices.* 44 (1997) 1529–1538. <https://doi.org/10.1109/16.622611>.
- [44] M.G. Ancona, H.F. Tiersten, Macroscopic physics of the silicon inversion layer, *Phys. Rev. B.* 35 (1987) 7959–7965. <https://doi.org/10.1103/PhysRevB.35.7959>.
- [45] M.G. Ancona, G.J. Iafrate, Quantum correction to the equation of state of an electron gas in a semiconductor, *Phys. Rev. B.* 39 (1989) 9536–9540. <https://doi.org/10.1103/PhysRevB.39.9536>.
- [46] H. Bartzsch, D. Glöb, P. Frach, M. Gittner, E. Schultheiß, W. Brode, J. Hartung, Electrical insulation properties of sputter-deposited SiO₂, Si₃N₄ and Al₂O₃ films at room temperature and 400 °C, *Phys. Status Solidi.* 206 (2009) 514–519. <https://doi.org/https://doi.org/10.1002/pssa.200880481>.
- [47] V. Leonov, C. Van Hoof, M. Goedbloed, R. Van Schaijk, Charge injection and storage in single-layer and multilayer inorganic electrets based on SiO₂ and Si₃N₄, *IEEE Trans. Dielectr. Electr. Insul.* 19 (2012) 1253–1260. <https://doi.org/10.1109/TDEI.2012.6259999>.
- [48] A.G. Aberle, Surface Passivation of Crystalline Silicon Solar Cells: A Review, *Prog. Photovoltaics Res. Appl.* 8 (2000) 473–487. https://doi.org/10.1007/978-3-319-75377-5_8.
- [49] A.G. Aberle, S. Glunz, W. Warta, Impact of illumination level and oxide parameters on Shockley-Read-Hall recombination at the Si-SiO₂ interface, *J. Appl. Phys.* 71 (1992) 4422–4431. <https://doi.org/10.1063/1.350782>.
- [50] B.E. Deal, M. Sklar, A.S. Grove, E.H. Snow, Characteristics of the Surface-State Charge (Q_{ss}) of Thermally Oxidized Silicon, *J. Electrochem. Soc.* 114 (1967) 266. <https://doi.org/10.1149/1.2426565>.
- [51] S.W. Glunz, A.B. Sproul, W. Warta, W. Wettling, Injection-level-dependent recombination velocities at the Si-SiO₂ interface for various dopant concentrations, *J. Appl. Phys.* 75 (1994) 1611–1615. <https://doi.org/10.1063/1.356399>.
- [52] S.W. Glunz, D. Biro, S. Rein, W. Warta, Field-effect passivation of the SiO₂/Si interface, *J. Appl. Phys.* 86 (1999) 683–691.
- [53] J.F. Verweij, J.H. Klootwijk, Dielectric breakdown I: A review of oxide breakdown, *Microelectronics J.* 27 (1996) 611–622. [https://doi.org/https://doi.org/10.1016/0026-2692\(95\)00104-2](https://doi.org/https://doi.org/10.1016/0026-2692(95)00104-2).

Extracting band-tail interface state densities from measurements and modelling of space charge layer resistance

Mingzhe Yu¹, Shona McNab¹, Isabel Al-Dhahir¹, Pietro P. Altermatt², and Ruy S. Bonilla^{1†}

¹Department of Materials, University of Oxford, Oxford, OX1 3PH, United Kingdom

²Trina Solar, State Key Laboratory for Photovoltaic Science and Technology (SKL PVST), Xinbei District, Changzhou, Jiangsu Province 213031, China

Supplementary materials

Table S1 and Table S2 show the calibrated positive and negative corona charge density at various corona discharge time at 30 kV.

Table S1. Calibrated positive corona charge density with corona discharge time.

Positive corona charge calibration	
Positive corona time (s)	Surface charge density (q/cm ²)
0	-2.589x10 ¹⁰
20	1.33x10 ¹²
40	2.69x10 ¹²
60	3.96x10 ¹²
80	5.13x10 ¹²
100	6.27x10 ¹²
130	7.91x10 ¹²
160	9.40x10 ¹²
190	1.11x10 ¹³

Table S2. Calibrated negative corona charge density with corona discharge time.

Negative corona charge calibration	
Negative corona time (s)	Surface charge density (q/cm ²)
0	-1.89x10 ¹⁰
5	-3.86x10 ¹¹
10	-7.07x10 ¹¹
15	-9.73x10 ¹¹
20	-1.21x10 ¹²
25	-1.46x10 ¹²
30	-1.71x10 ¹²
35	-1.96x10 ¹²

† Corresponding author: sebastian.bonilla@materials.ox.ac.uk

1
2
3
4
5
6
7
8
9
10
11
12
13
14
15
16
17
18
19
20
21
22
23
24
25
26
27
28
29
30
31
32
33
34
35
36
37
38
39
40
41
42
43
44
45
46
47
48
49
50
51
52
53
54
55
56
57
58
59
60
61
62
63
64
65

40	-2.20×10^{12}
45	-2.46×10^{12}
50	-2.71×10^{12}
55	-2.93×10^{12}
60	-3.20×10^{12}
65	-3.42×10^{12}
70	-3.65×10^{12}
75	-3.92×10^{12}
80	-4.13×10^{12}
85	-4.37×10^{12}
90	-4.63×10^{12}

Extracting band-tail interface state densities from measurements and modelling of space charge layer resistance

Mingzhe Yu¹, Shona McNab¹, Isabel Al-Dhahir¹, Christopher E. Patrick¹, Pietro P. Altermatt², and Ruy S. Bonilla^{1*}

¹Department of Materials, University of Oxford, Oxford, OX1 3PH, United Kingdom

²Trina Solar, State Key Laboratory for Photovoltaic Science and Technology (SKL PVST), Xinbei District, Changzhou, Jiangsu Province 213031, China

$$D_{it}(CB, acceptor) = D_{it}(max, CB, acceptor) \times e^{-\frac{(1.1-E)}{E_{CB,trap}}} \quad (1)$$

$$D_{it}(VB, donor) = D_{it}(max, VB, donor) \times e^{-\frac{E}{E_{VB,trap}}} \quad (2)$$

$$R_S(wafer) = \frac{1}{\int_0^{thickness} (nq\mu_n + pq\mu_p) dt} \quad (3)$$

Table 1. Summary of parameters used for simulation of wafer sheet resistance in the presence of dielectric charge in Sentaurus TCAD.

Parameter	Value
Wafer thickness	200 μm
Bulk base resistivity	n-type, 0.96-1.04 Ωcm
SRH bulk lifetime	$\tau_n = 0.371 \text{ ms}$, $\tau_p = 3.71 \text{ ms}$
Dielectric charge density	$-9 \times 10^{12} - 9 \times 10^{12} \text{ cm}^{-2}$
D_{it} (midgap)	$5 \times 10^{10} - 10^{13} \text{ eV}^{-1}\text{cm}^{-2}$
D_{it} (max, CB, acceptor)	CB: $10^{13} - 6 \times 10^{15} \text{ eV}^{-1}\text{cm}^{-2}$ VB: $10^{13} - 3 \times 10^{15} \text{ eV}^{-1}\text{cm}^{-2}$

Table 2. Details of parameters used in simulations for best fits with experimental wafer sheet resistance vs. charge density curves of Set 1 samples.

	10 nm oxide, FGA		100 nm oxide			100 nm oxide, FGA	
	Sample 1	Sample 2	Sample 1	Sample 2	Sample 3	Sample 1	Sample 2
Wafer resistivity	1.053	1.049	1.045	1.044	1.03	1.016	1.01
D_{it} (max, CB, acceptor)	5.5×10^{13}	4×10^{13}	1.02×10^{14}	5×10^{13}	1.44×10^{14}	1.38×10^{14}	9.1×10^{13}
N_{it} (acceptor)	3.54×10^{12}	$< 2.57 \times 10^{12}$	6.56×10^{12}	$< 3.21 \times 10^{12}$	9.26×10^{12}	8.87×10^{12}	5.85×10^{12}

* Corresponding author: sebastian.bonilla@materials.ox.ac.uk

Table 3. Details of parameters used in simulations for best fits with experimental wafer sheet resistance vs. charge density curves of Set 2 samples.

	Si/SiO ₂		Si/SiO ₂ /SiN _x	
	Sample 1	Sample 2	Sample 1	Sample 2
Wafer resistivity	8.65	8.45	8.2	
D_{it} (max, CB, acceptor)	3.2x10 ¹⁴		2.2x10 ¹⁴	
N_{it} (acceptor)	2.09x10 ¹³		1.44x10 ¹³	

Supplementary materials

Table S1. Calibrated positive corona charge density with corona discharge time.

Positive corona charge calibration	
Positive corona time (s)	Surface charge density (q/cm ²)
0	-2.589x10 ¹⁰
20	1.33x10 ¹²
40	2.69x10 ¹²
60	3.96x10 ¹²
80	5.13x10 ¹²
100	6.27x10 ¹²
130	7.91x10 ¹²
160	9.40x10 ¹²
190	1.11x10 ¹³

Table S2. Calibrated negative corona charge density with corona discharge time.

Negative corona charge calibration	
Negative corona time (s)	Surface charge density (q/cm ²)
0	-1.89x10 ¹⁰
5	-3.86x10 ¹¹
10	-7.07x10 ¹¹
15	-9.73x10 ¹¹
20	-1.21x10 ¹²
25	-1.46x10 ¹²
30	-1.71x10 ¹²
35	-1.96x10 ¹²
40	-2.20x10 ¹²
45	-2.46x10 ¹²
50	-2.71x10 ¹²
55	-2.93x10 ¹²
60	-3.20x10 ¹²

65	-3.42×10^{12}
70	-3.65×10^{12}
75	-3.92×10^{12}
80	-4.13×10^{12}
85	-4.37×10^{12}
90	-4.63×10^{12}

Extracting Band-tail Interface State Densities from Measurements and Modelling of Space Charge Layer Resistance

Mingzhe Yu¹, Shona McNab¹, Isabel Al-Dhahir¹, Christopher E. Patrick¹, Pietro P. Altermatt², and Ruy S. Bonilla^{1*}

¹Department of Materials, University of Oxford, Oxford, OX1 3PH, United Kingdom

²Trina Solar, State Key Laboratory for Photovoltaic Science and Technology (SKL PVST), Xinbei District, Changzhou, Jiangsu Province 213031, China

Abstract- Dielectric-silicon interfaces are becoming ever more important to device performance.

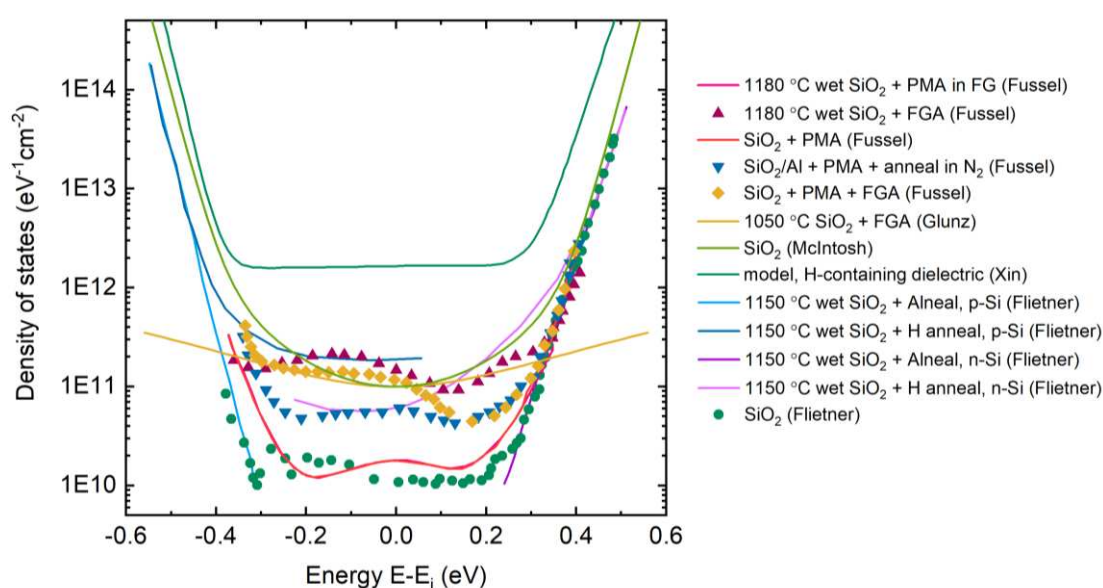


Figure 1. Density of states distribution of various Si/SiO₂ interfaces, redrawn from [11,17,20,22,23,33]. PMA: post metallization anneal; FGA: forming gas anneal; FG: forming gas.

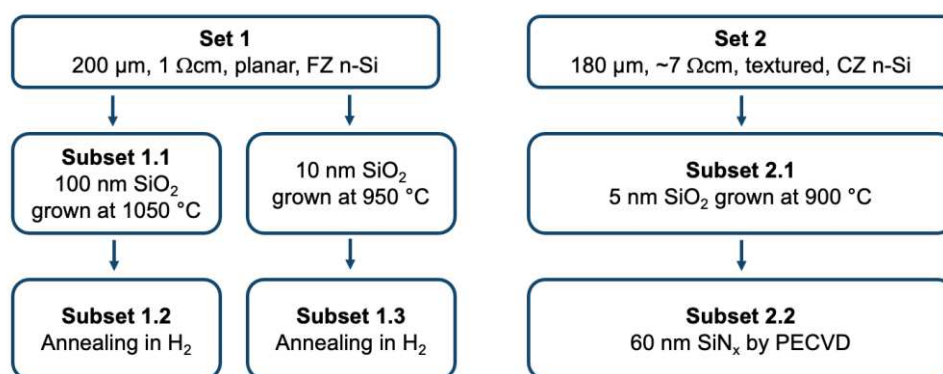


Figure 2. Detailed processing of Set 1 and Set 2 samples.

* Corresponding author: sebastian.bonilla@materials.ox.ac.uk

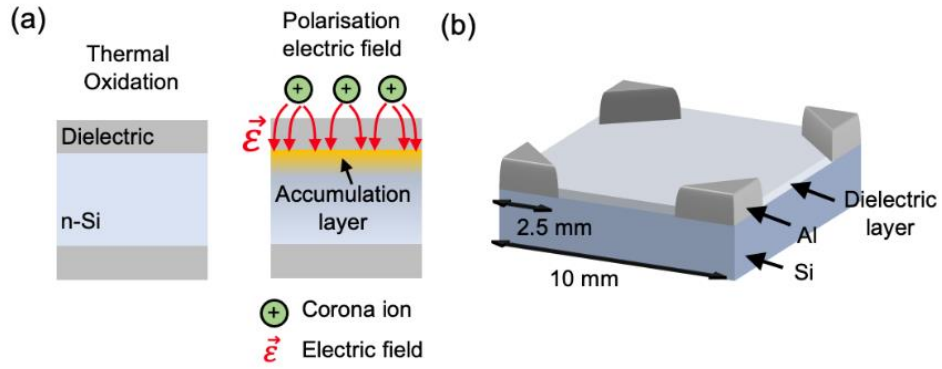


Figure 3. (a) Processing method and schematic of a corona ion-deposited n-Si wafer. (b) Sample structure for Van der Pauw measurement.

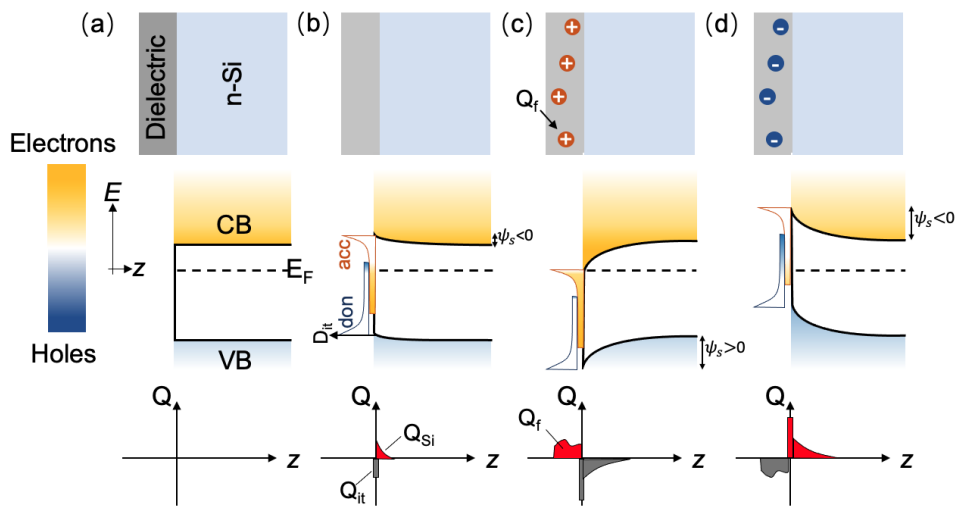


Figure 4. Schematic energy diagram at an n-Si/SiO₂ interface at (a) an ideal neutral state, (b) in the presence of charged donor and acceptor interface states, and in the presence of (c) positive or (d) negative dielectric charge. Redrawn from [38].

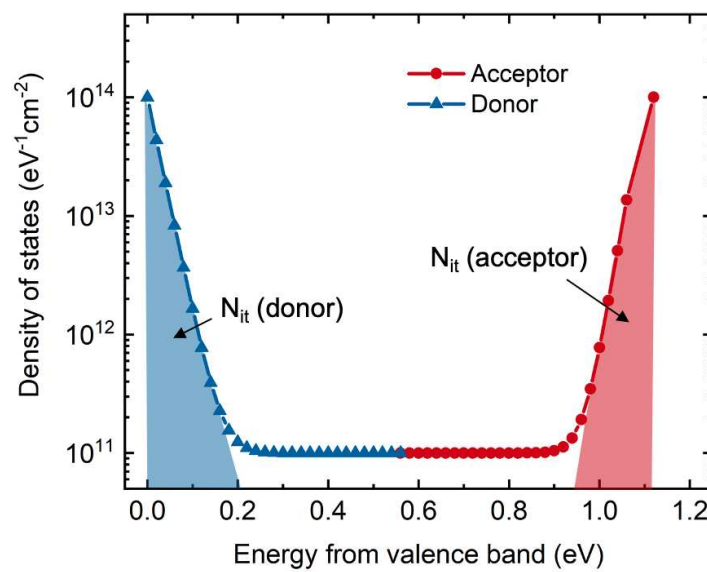


Figure 5. Density of states distribution at Si/SiO₂ interface in a model with D_{it} being 10¹¹, 10¹⁴, and 10¹⁴ eV⁻¹cm⁻² at midgap, conduction band edge, and valence band edge.

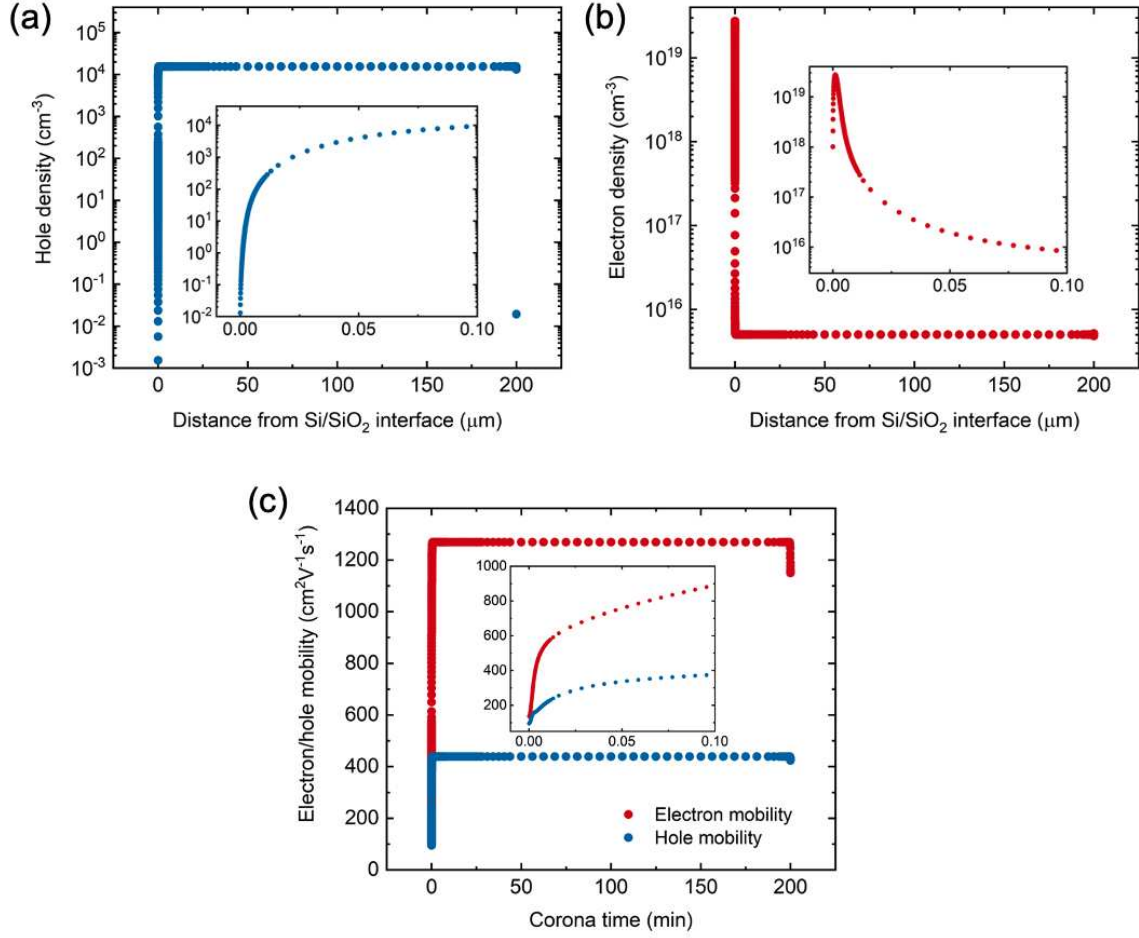


Figure 6. Simulated carrier density including (a) electrons and (b) holes. (c) Carrier mobility across the whole wafer extracted from a n-type, $1\ \Omega\text{cm}$ model with positive charge density of $9 \times 10^{12}\ \text{cm}^{-2}$ at the front dielectric. D_{it} is 10^{11} , 10^{14} , and $10^{14}\ \text{eV}^{-1}\text{cm}^{-2}$ at midgap, conduction band edge, and valence band edge in the model.

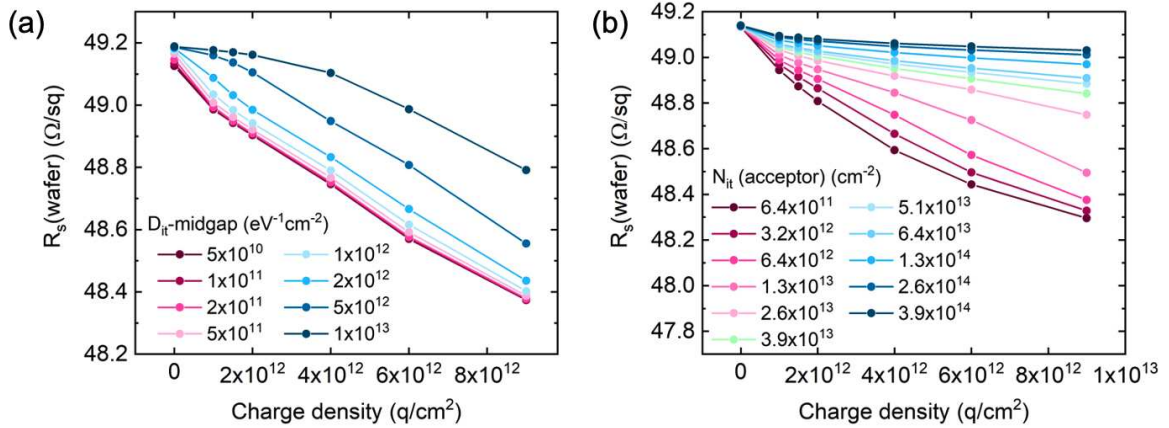


Figure 7. Simulated wafer sheet resistance vs. positive charge density curves of a $200\ \mu\text{m}$ thick, $1\ \Omega\text{cm}$ n-Si substrate at various (a) D_{it} (midgap), and (b) N_{it} (acceptor) near conduction band edge.

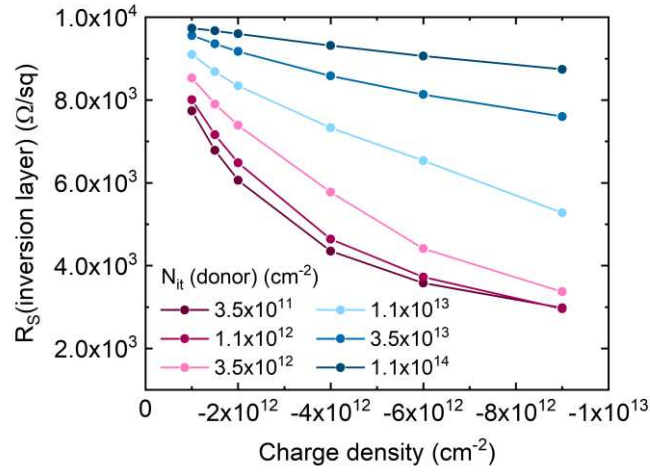


Figure 8. Simulated inversion layer sheet resistance vs. negative charge density of a 200 μm thick, 1 Ωcm n-Si substrate at various N_{it} (donor) near valence band edge.

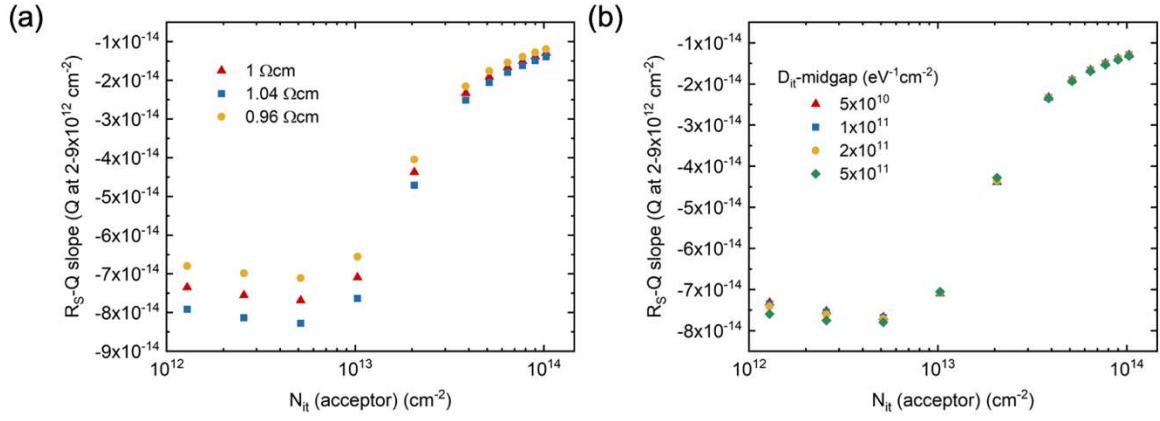


Figure 9. Slope of simulated wafer sheet resistance vs. positive charge density curve on a 200 μm thick, 1 Ωcm n-Si substrate at charge density in the range of 2 - 9x10¹² cm⁻², as a function of N_{it} (acceptor), with varied (a) wafer resistivity, and (b) D_{it} (midgap).

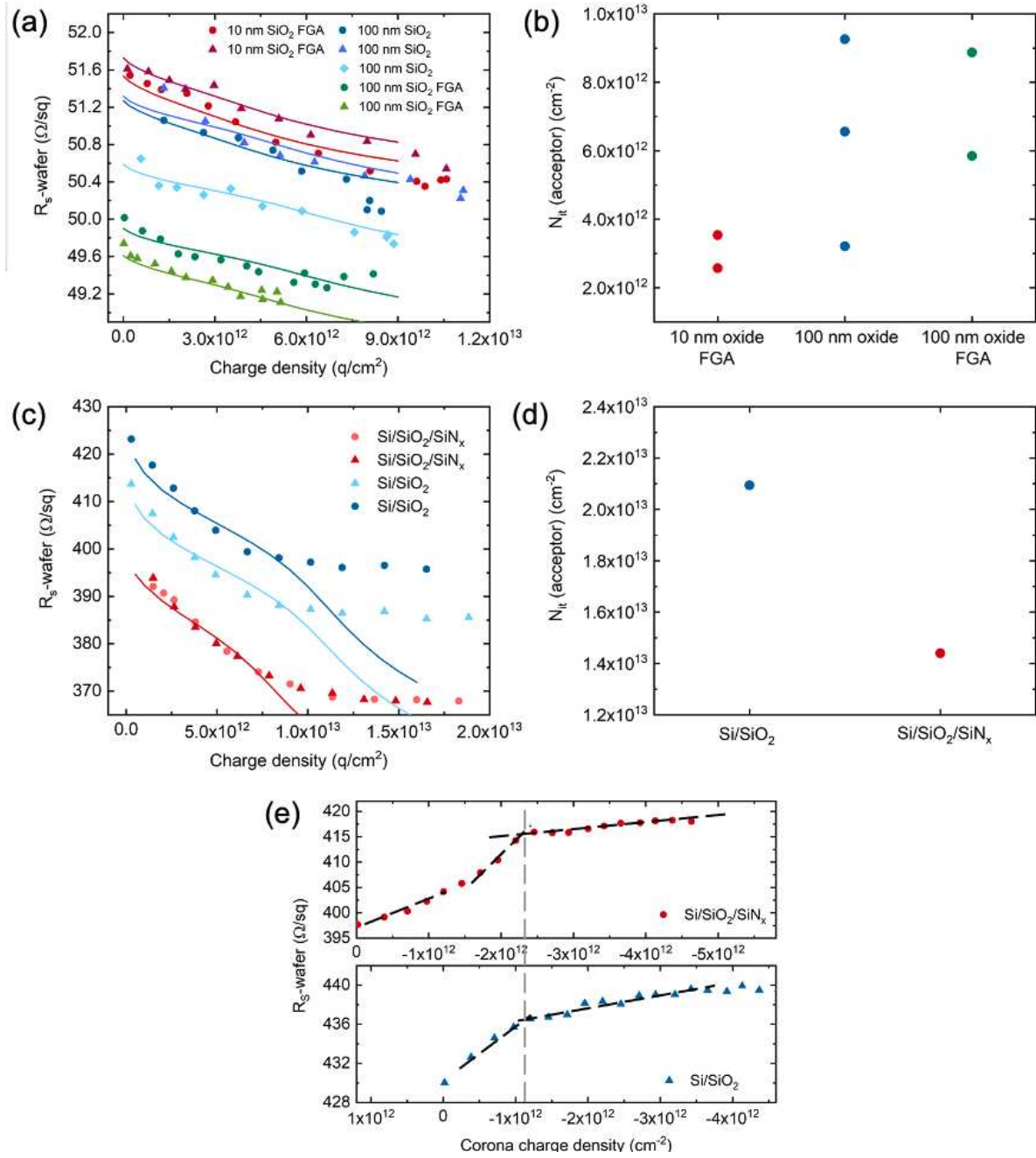


Figure 10. (a) Experimental (symbols) and simulated (lines) wafer sheet resistance vs. positive charge density curves, and (b) extracted N_{it} (acceptor) for Set 1 samples. (c) Experimental and simulated wafer sheet resistance vs. positive charge density curves, and (d) extracted N_{it} (acceptor) for Set 2 samples. (e) Wafer sheet resistance vs. negative charge density curves of Set 2 samples.